

Solar Wind Forecasting with Coronal Holes

S. Robbins¹, C. J. Henney² and J. W. Harvey²

¹*APS Department, University of Colorado, Boulder, CO 80309, USA*

²*National Solar Observatory, Tucson, Arizona, 85719, USA*

Abstract. An empirical model for forecasting solar wind speed related geomagnetic events is presented here. The model is based on the estimated location and size of solar coronal holes. This method differs from models that are based on photospheric magnetograms (e.g., Wang-Sheeley model) to estimate the open field line configuration. Rather than requiring the use of a full magnetic synoptic map, the method presented here can be used to forecast solar wind velocities and magnetic polarity from a single coronal hole image, along with a single magnetic full-disk image. The coronal hole parameters used in this study are estimated with Kitt Peak Vacuum Telescope He I 1083 nm spectrograms and photospheric magnetograms. Solar wind and coronal hole data for the period between May 1992 and September 2003 are investigated. The new model is found to be accurate to within 10% of observed solar wind measurements for its best one-month periods, and it has a linear correlation coefficient of ~ 0.38 for the full 11 years studied. Using a single estimated coronal hole map, the model can forecast the Earth directed solar wind velocity up to 8.5 days in advance. In addition, this method can be used with any source of coronal hole area and location data.

1. Introduction

Prediction of space weather near the Earth is a major goal of solar research. An important aspect of attaining this goal is to accurately describe the solar drivers of space weather. The drivers are the solar wind and the various phenomena that shape and modulate that wind. Among the earliest findings from space observations of the solar wind was that it consisted of recurrent low-speed, dense streams and high-speed tenuous streams, and that the latter were strongly associated with increased geomagnetic activity (Synder, Neugebauer, and Rao, 1963). Many suggestions were made that the high-speed solar wind streams might be associated with regions on the Sun having magnetic fields open to interplanetary space.

When coronal holes were found to be regions likely to have open magnetic fields (Altschuler, Trotter, and Orrall, 1972), it was not long until Krieger, Timothy, and Roelof (1973), and several other investigators, demonstrated a link between open-field coronal holes, high-speed solar wind streams, and enhanced geomagnetic activity. In an effort to strengthen this linkage, Sheeley, Harvey, and Feldman (1976) constructed time-stacked diagrams of coronal holes, solar wind speed and



© 2018 Kluwer Academic Publishers. Printed in the Netherlands.

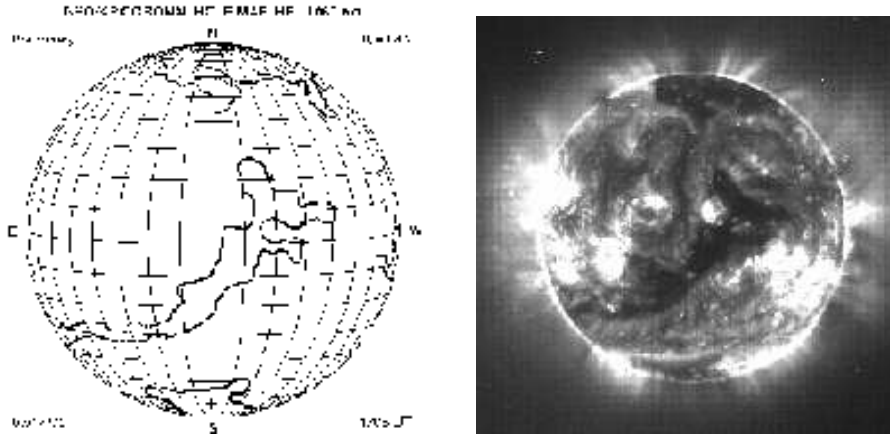


Figure 1. A sample NSO/KPVT computer-assisted hand-drawn coronal hole image (left) and a EIT 19.5 nm Fe XII emission line image (left) for July 14, 2003 at approximately 17 UT. Note that the coronal hole regions appear dark in the EIT image.

geomagnetic activity in one-rotation-long rows. The diagrams covering the years 1973-1975 strongly supported the linkage and the authors suggested that observations of coronal holes could be used to predict the arrival of high-speed streams and their associated geomagnetic activity a week in advance.

Coronal holes are best seen against the solar disk as low-intensity regions in space observations of material at coronal temperatures. This can also be done from the ground using radio observations. Harvey et al. (1975) found that coronal holes could be seen faintly in ground-based images made with helium lines such as 587.6 and 1083.0 nm because the strength of these lines is partly controlled by the intensity of overlying coronal radiation (see, e.g., Andretta and Jones, 1997). A program of regular 1083 nm observations has been conducted by the National Solar Observatory (NSO) Kitt Peak Vacuum Telescope (KPVT) starting in 1974. Among the derived products are estimates of the locations and magnetic polarity of coronal holes. An example coronal hole estimate image derived from a KPVT observation is shown in Figure 1, along with a 19.5 nm Fe XII emission line image measured by the Extreme Ultraviolet Imaging Telescope (EIT) for comparison. Harvey and Recely (2002) describe how coronal holes are identified using KPVT He I 1083 nm observations.

Predictions of solar wind speed at Earth are regularly made by several groups based on solar potential field extrapolations (e.g., <http://solar.sec.noaa.gov/ws/>, <http://www.lmsal.com/forecast/>, <http://bdm.iszf.irk.ru/Vel.html>, and <http://gse.gi.alaska.edu>) and in-

terplanetary scintillation (Hewish et al., 1964) observations (e.g., <http://cassfos02.ucsd.edu/solar/forecast/index.html>, and <http://stesun5.stelab.nagoya-u.ac.jp/forecast/>). The former set of forecasts are based on extrapolation of photospheric longitudinal magnetic field measurements using a potential field assumption to locate open field lines. Using one of these models, a modified Wang and Sheeley (1990, 1992) flux-transport model, Arge and Pizzo (2000) studied a three-year period centered about the May 1996 solar minimum. They compared predicted solar wind speed and magnetic polarity with observations near Earth. Their three-year sample period had an overall correlation of ~ 0.4 with observed solar wind velocities and an average fractional deviation, ξ , of 0.15, where $\xi = \langle (\text{prediction} - \text{observed}) / \text{observed} \rangle$. When excluding a 6-month period with large data gaps, they correctly forecast the solar wind to within 10 – 15%. Interplanetary magnetic field (IMF) polarity was correctly forecast $\sim 75\%$ of the time.

In this paper, we address the suggestion of Sheeley, Harvey, and Feldman (1976) that observations of coronal hole regions can be used to predict the solar wind speed at Earth as much as a week in advance. In addition, the model presented here is based on observations that find moderate and high-speed solar wind streams are associated with small and large near-equatorial coronal holes, respectively (Nolte et al., 1976). Here we correlate the coronal hole percent area coverage of sectoral regions of the observed solar surface with solar wind measurements to derive a simple empirical model (discussed in Sections 2 through 5). As a measure of the merit of this model for solar wind forecasting, we compare predictions with observations and contrast this technique with the ones based on magnetic field extrapolations (Sections 5 and 6).

2. Model Input Data

The coronal hole data used here are based on KPVT observations from May 28, 1992 through September 25, 2003 (i.e. the last half of cycle 22 and the first half of cycle 23). The coronal hole locations and area estimates are from computer-assisted, hand-drawn maps (see Figure 1) based upon the KPVT He I 1083 nm images and photospheric magnetograms (Harvey and Recely, 2002). For this investigation, the estimated coronal hole boundaries were mapped into sine-latitude and longitude to create heliographic images. The coronal hole region image pixels are set to a value of 1, whereas the background is defined as 0. For the time period analyzed here, the KPVT coronal hole maps have a 69% daily coverage.

The solar wind speed data utilized here was obtained from the OMNIWeb website (<http://nssdc.gsfc.nasa.gov/omniweb/>) provided by the National Space Science Data Center. Daily averages of the solar wind speed time series were created with the approximate cadence of the KPVT-based coronal hole maps. For the time period analyzed here, the solar wind speed time series has a 92% daily coverage. Data gaps in the time series are interpolated using a cubic spline.

3. Solar Wind Correlation Analysis

For comparison with the solar wind speed time series, each heliographic coronal hole image was divided into 23 swaths (i.e. sectoral regions) 14 degree-wide in longitude overlapped by 7 degrees. The approximately 1-day-wide longitudinal window was selected to correspond with the temporal cadence of the KPVT observations. These sectoral samples are then summed, where each pixel corresponding to a coronal hole is equal to 1, to yield a percent coverage of that area by coronal holes. For each coronal hole image there may be no or only a few coronal hole regions observed for that time. For example, swath sectors with no coronal hole regions would yield a hole coverage of zero percent. This is repeated for each coronal hole image available in the 11-year period to form a coronal hole time series for each of the 23 sectoral samples. Each sectoral time series is then interpolated into the time frame of the solar wind velocity data.

The correlation and time lag between the time series were estimated with weighted cross-correlations (e.g. Bevington and Robinson, 2003). The weighted cross-correlation simplifies the analysis by allowing the use of the continuous time series. The gap-filled data are given small weights to minimize their contribution while the measured or derived values are given equal and relatively large weight values. In addition, following Arge et al. (2004), periods of CME events were estimated using the plasma β value (obtained from the OMNIWeb data set) when $\beta \leq 0.1$. For periods estimated to correspond to a coronal mass ejection (CME) event, solar wind speed values were given negligible weight values.

3.1. LONGITUDINAL FORECASTING WINDOWS

Twenty-three longitude swaths were examined, ranging from 77 degrees east to 77 degrees west of the central meridian. Each of these was cross-correlated with the solar wind speed time series in the manner described above. Figure 2 exhibits the maximum cross-correlation coefficient within a lag window of ± 0.5 days for each longitude swath

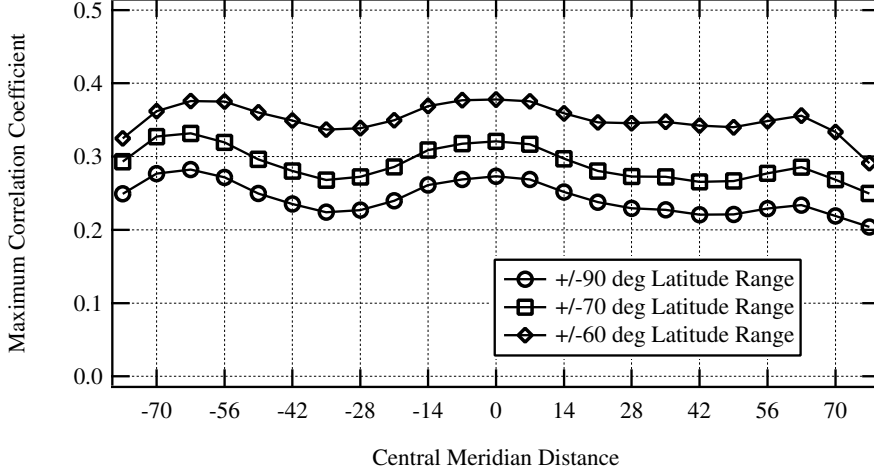


Figure 2. Longitude Cross-Correlations: 14 degree-wide swaths of the solar disk were tiled across the solar surface with 7 degrees overlap between successive swaths for 3 latitude ranges. The maximum cross-correlations within a lag window of ± 0.5 days (corresponding to a day offset described by Equation (1)) of the resulting data set with the solar wind velocity data are shown here. Negative and positive longitude values correspond to eastward (E) and westward (W) respectively. Note the two relatively good forecast windows centered around 63 degrees east and the central meridian. The correlations continue to improve with model time series using decreasing latitude ranges, peaking with the latitude range of ± 60 degrees. The trend reverses for latitude ranges narrower than ± 60 degrees.

investigated with the latitude ranges ± 90 degrees, ± 70 degrees, and ± 60 degrees with equal latitude weights. Note that besides the central meridian peak, the correlation also peaks towards the east and west limbs. This is a result of better coronal hole detection from the KPVT He I 1083 nm spectroheliograms towards the image limb. In addition to the three latitude bands shown in Figure 2, the correlation values were also determined for ± 50 and ± 40 deg cases. These two latitude bands are similar to the ± 60 degree case but have lower correlation values eastward of -56 degrees. For the ± 60 deg case, two preferred forecasting windows centered at 63 degrees east and on the central meridian are clearly visible.

The estimated swath time series lags corresponding to maximum cross-correlation coefficients are found to be linear, and can be expressed as:

$$d = (3.69 \pm 0.02) - (0.07386 \pm 0.0005) \theta, \quad (1)$$

where d is the time delay in days and θ is the center of the longitude swath in degrees as measured from the central meridian (east is neg-

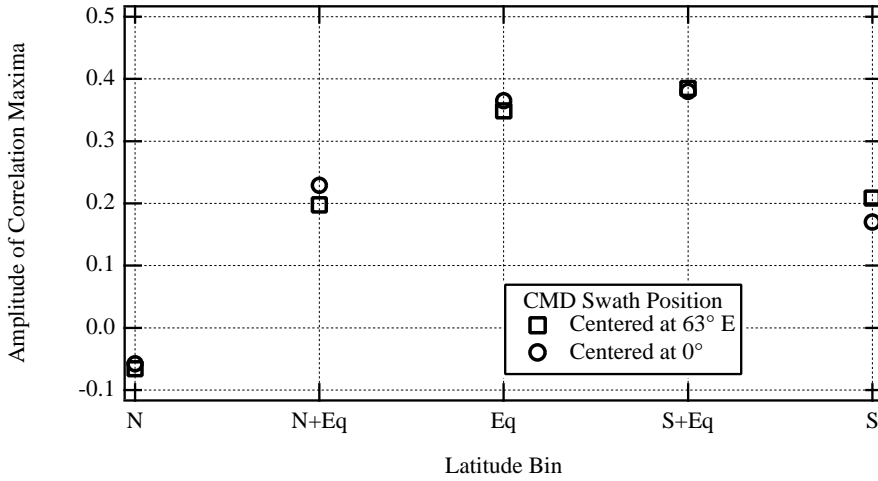


Figure 3. The two longitude forecasts’ cross-correlations with the solar disk divided into five latitude regions described in §3.2. See text for discussion.

ative, west is positive) and the uncertainty values are $1-\sigma$. Note that Equation (1) is valid within the central meridian distance range of -80 to 80 degrees, but it only has physical meaning (days forecast) for the central meridian distance range of -80 to 40 degrees. From Equation (1), the two preferred forecasting windows centered at 63 degrees east and on the central meridian (see Figure 2), the time lags of these forecasts correspond to 8.3 days and 3.7 days respectively. In other words, the delay between detected solar wind variations at Earth and a coronal hole region at the central meridian ($\theta = 0$ degrees) is approximately 3.7 days. A coronal hole region observed at 63 degrees east central meridian distance ($\theta = -63$ degrees) is associated to solar wind speed variations at Earth approximately 8.3 days later. The observed delay is as expected, and is best explained as the result of a corotating stream of plasma moving nearly radially outward from the sun (e.g. Gosling, 1996).

3.2. LATITUDE WEIGHTING ANALYSIS

In addition to the longitudinal correlation analysis above, the heliographic coronal hole images were divided into three latitude bins: Northern (90 degrees north to 30 degrees north), Equatorial (30 degrees north to 30 degrees south), and Southern (30 degrees north to 90 degrees south) regions. Combinations of Northern with Equatorial and Southern with Equatorial were used for a total of five bins. The cross-correlation coefficient values of each latitude bin were calculated for the two longitudinal windows discussed in §3.1.

The amplitude of the correlation coefficient maxima shown in Figure 3 reveals a bias towards the southern hemisphere. This bias in the cross-correlation between the hemispheres is most likely due to the significantly greater number of coronal holes detected in the southern hemisphere for the period investigated (e.g. Henney and Harvey, 2005). Assuming that the hemispheric asymmetry is a result of the limited distribution sample of coronal holes, and following the analysis discussed in the previous section, the latitude range of ± 60 degrees was used for the forecasting analysis done below. The maximum weighted cross-correlations for the East window was 0.376 and the central meridian had a correlation of 0.378 (see Figure 2).

A model solar wind time series, V_{mod} , is created by first determining the area percentage of the 14-degree wide sectors that is a coronal hole, I_s . These coronal hole percentage values for each longitudinal swath are rescaled to agree with the observed solar wind speed, V_{obs} , using the linear scaling coefficients α and γ , where $V_{\text{mod}} = \alpha + \gamma I_s$. The linear scaling coefficients were determined by minimizing the mean of the absolute average fractional deviation, ξ , of the model from the observed values, where

$$\xi = \langle (V_{\text{obs}} - V_{\text{mod}}) / V_{\text{obs}} \rangle. \quad (2)$$

Using the above criteria and a latitude range of ± 60 degrees, the average linear scaling values for each longitude window are found to be: $\alpha = 330$ km/s and $\gamma = 930$ km/s. With these scaling factors and the best weighting as discussed above, the resulting ξ for the entire 11-year data set for the central meridian swath is $\sim 16\%$ with a standard deviation of $\pm 20\%$.

4. Magnetic Activity Cycle Dependence

Sheeley and Harvey (1981) reported a dependence between the coronal hole and solar wind correlation and the sunspot cycle. This was quantitatively explored for the time period spanned by the coronal hole data set - the last half of cycle 22 and the first half of cycle 23. The full time series was divided into six time series of approximately 690 days, illustrated in the upper graph in Figure 4 with sunspot number time series (sunspot count data used here was obtained from the NGDC website (<http://www.ngdc.noaa.gov/stp/>), maintained by the National Geophysical Data Center). The date range and percent coverage of the six periods are outlined in Table I.

Figure 4 highlights a strong dependence of the time series correlation values on the phase of the sunspot cycle, similar to the qualitative

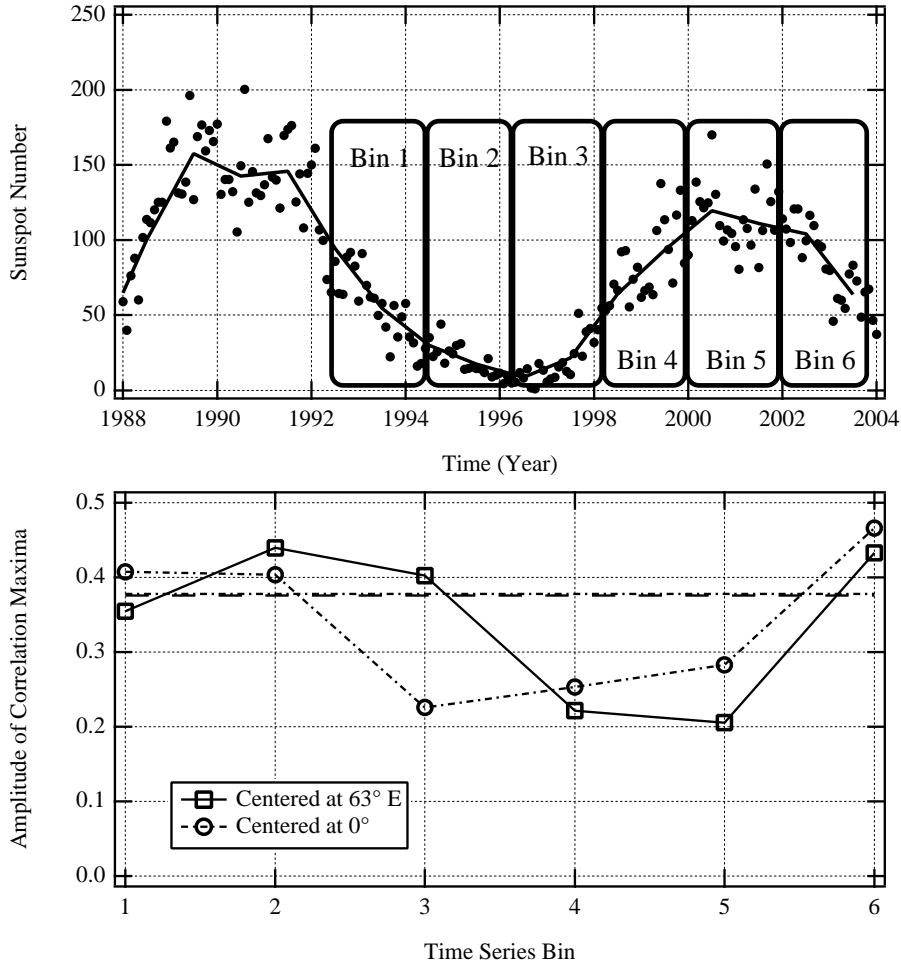


Figure 4. Monthly (solid dots) and yearly (line) sunspot number averages are shown in the upper panel along with six time bins into which the 11-year data set was divided. The six bins are indicated by the rounded rectangles and each represents a duration of approximately 690 days. Date ranges for each period are listed in Table I. Shown in the lower panel are the cross-correlation values of the coronal hole data with the solar wind for the 6 intervals illustrated in the upper figure. The correlation is found to be best during the declining phase of the sunspot cycle and worst just after solar minimum.

results of Sheeley and Harvey (1981). The correlation between the coronal hole and solar wind time series is best during the declining phase of the cycle, and it is worst during solar minimum and the beginning ascending phase of the cycle. Some of the lack of correlation can be attributed to the observed latitudinal distribution of coronal holes with respect to the solar cycle. During the minimum phase of the

Table I. Time series subdivisions used in the cross-correlation analysis relative to the sunspot number time series shown in Figure 4.

Period Bin	Date Range	Interval (days)	Completeness
1	May 28, 1992 - Apr 17, 1994	690	66.1%
2	Apr 18, 1994 - Mar 7, 1996	690	68.4%
3	Mar 8, 1996 - Jan 26, 1998	690	72.2%
4	Jan 27, 1998 - Dec 17, 1999	690	73.8%
5	Dec 18, 1999 - Nov 6, 2001	690	64.6%
6	Nov 7, 2001 - Sep 25, 2003	688	66.3%
1 - 6	May 27, 1992 - Sep 25, 2003	4138	68.6%

solar cycle, fewer low-latitude coronal holes are observed which means few fast streams are observed by spacecraft in the ecliptic plane (e.g. Woch et al., 1997; Kojima et al., 2001; Kojima et al., 2004).

However, the source of the poor correlation during solar minimum is also likely a result of a noted difficulty in the determination of coronal hole regions using He I 1083 nm spectroheliograms during periods of low magnetic activity. Both longitude windows vary over approximately the same range throughout the cycle, and even though during the worst forecasting period the correlation is far below the full time series' average, it is still well above statistical significance. Correlation significance, the probability that two uncorrelated random sets of variables with a given number of observations would give similar correlation values, was calculated following Appendix C in Bevington and Robinson (2003). The correlation is considered highly significant and nominally significant if the probability of chance occurrence is less than 1% and 5%, respectively (Taylor, 1997).

The time delays between coronal hole observation and the effects seen in the solar wind velocity are slightly longer during solar minimum and slightly shorter during solar maximum than the averages quoted in §3.1. The lags range over 8.38 ± 0.34 and 3.82 ± 0.58 days.

5. IMF Polarity Forecast

Besides area and position information, the Harvey and Recely (2002) coronal hole boundary images include magnetic polarity. So, in addition to forecasting the solar wind velocity, the KPVT estimated coronal hole maps can be used to predict the interplanetary magnetic field (IMF) polarity at Earth. The longitudinal swath centered at the central

meridian, the 3.7-day forecast, was used in the following analysis. The heliographic coronal hole maps are scaled so that each pixel with a positive polarity hole has a value of $+1$ and each pixel with a negative polarity hole has a value of -1 , whereas non-coronal hole regions are set to 0. The average value of all the pixels in the 14 degree wide swath was taken, with a range between ± 60 degrees in latitude. The averaging of the coronal hole polarity, albeit simple, is treated here as a baseline for the polarity forecasting when using only coronal hole regions.

Excluding only the days that did not have both velocity and coronal hole data, leaving 63.0% of the comparison period, the IMF polarity was correctly forecast 57.9% of the time. When excluding an additional 17.9% of the days where the average model magnetic polarity was within 0.1% of 0, the IMF polarity is correctly forecast for 63.5% of the time. This is approximately 10% lower than the values reported by Arge and Pizzo (2000); however, we expect improvement with future models. Though the current model has inherent inaccuracies as a result of the oversimplification of the magnetic field structure associated with coronal holes and the resulting solar wind, the use of higher signal-to-noise ratio magnetograms is expected to improve the polarity forecast. In addition, this model is partly based on the assumption that the solar wind velocity is related linearly with the size of the coronal hole. However, it has been shown that there is a critical scale size for which the wind velocity is independent of coronal hole size (Kojima et al., 2004). In future models, we plan to include coronal hole size and additional topology-related parameters to potentially improve forecasts.

6. Forecast Comparison and Discussion

Figure 5 illustrates two sample forecast periods that cover two Carrington rotations (CR) each: CR 1862 and 1863 (top), and CR 1955 and 1954 (bottom). To objectively find periods of good and bad forecasts, both weighted cross-correlations for 90-day periods as well as absolute average fractional deviations, see Equation (2), were performed. For each time series, only valid data (non-gap-filled data values) are shown in the figures. Ranges quoted in this section are from the two different forecast windows (discussed in §3) centered at 63 degrees east and 0 degrees relative to the central meridian.

The top forecast comparison shown in Figure 5 is a sample period when the model time series is well-correlated with the solar wind speed data. For the two forecast windows, the weighted correlation coefficients range from 0.626 to 0.698, and the absolute average fractional deviation, ξ , is found to be 0.098. In comparison, the best one-month

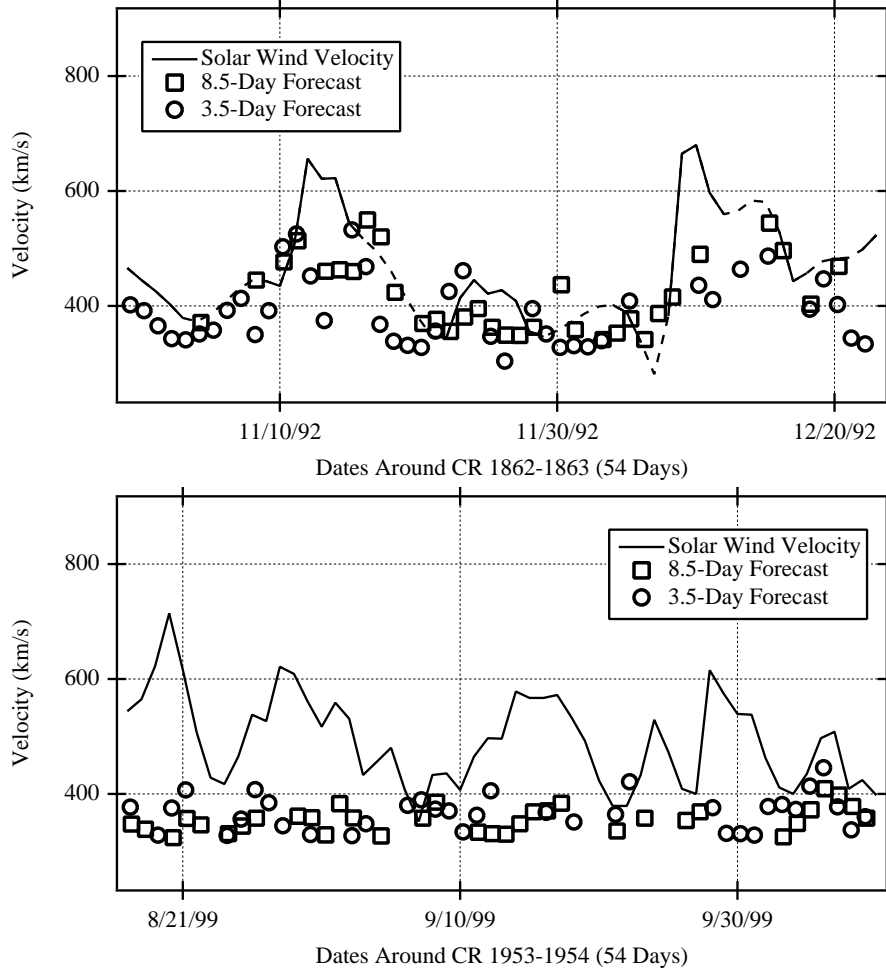


Figure 5. A good forecast (top) comparison relative to a representative poor forecast (bottom) comparison between the model estimates (symbols) and the measured solar wind speed (solid line). In the top forecast, dotted lines are interpolated solar wind speed values.

period studied by Arge and Pizzo (2000) has an unweighted correlation of 0.813 and an absolute average fractional deviation of 0.159. The bottom forecast comparison shown in Figure 5 illustrates an example of a poor cross-correlation between the two longitude windows and the solar wind velocity, ranging from 0.113 to 0.179. This is below statistical significance for the forecast comparison period of 54 days (shown in Figure 5). The absolute average fractional deviation ranges from 0.207 to 0.245 for this period.

For the three-year period studied by Arge and Pizzo (2000), they found, using their best forecast method, a correlation of 0.389, whereas the entire 11 years studied here has a weighted correlation range of 0.376 to 0.378 depending on longitudinal window used. In addition, Arge and Pizzo (2000) reported an absolute average fractional deviation, ξ , for the three years studied of 0.15. The best absolute average fractional deviations for a one-month period presented in their paper was 0.096. The weighted ξ for the best one-month periods studied here ranged between 0.073 and 0.076 for the two forecast windows. Months with less than 10 days for which the data sets overlapped after weighting were excluded. For the approximate 137 months studied in this paper, the mean ξ ranged between 0.167 and 0.176 with a standard deviation of about 0.051.

Near term plans include applying the forecasting model presented here to SOLIS-VSM (Vector Spectromagnetograph) estimated coronal hole images derived from daily full-disk photospheric magnetograms and He I 1083 nm spectroheliograms using an automated coronal hole detection algorithm developed by Henney and Harvey (2005).

7. Conclusion

The empirical solar wind forecasting model presented here is based on the location and size of solar coronal holes. From a single coronal hole area image, along with a single magnetogram, this method can be used to forecast solar wind velocities and polarity up to 8.5 days in advance with a mean wind speed deviation as low as 9.6% for a given one-month period. The model is found to be accurate to within 10% of observed solar wind measurements for its best one-month periods. Possible improvements include adding the estimated quality of the coronal hole area determination, along with weighting by the size and topology of each coronal hole, used as input to the model.

8. Acknowledgments

The coronal hole data used here was compiled by K. Harvey and F. Recely using NSO KPVT observations under a grant from the National Science Foundation (NSF). NSO Kitt Peak data used here are produced cooperatively by NSF/AURA, NASA/GSFC, and NOAA/SEL. The EIT data is courtesy of the SOHO/EIT consortium. SOHO is a project on international cooperation between ESA and NASA. Solar wind and plasma β data used here is available online at <http://nssdc.gsfc.nasa.gov/omniweb/>.

Sunspot data used here is available online at <http://www.ngdc.noaa.gov/stp/>. This work is carried out through the NSO Research Experiences for Undergraduate (REU) site program, which is co-funded by the Department of Defense in partnership with the NSF-REU Program. This research was supported in part by the Office of Naval Research Grant N00014-91-J-1040. The NSO is operated by AURA, Inc. under a cooperative agreement with the NSF.

References

- Altschuler, M. D., Trotter, D. E., and Orrall, F. Q.: 1972, *Solar Phys.* **26**, 354.
- Andretta, V. and Jones, H. P.: 1997, *Astrophys. J.* **489**, 375.
- Arge, C. N., Luhmann, J. G., Odstrcil, D., Schrijver, C. J., and Li, Y.: 2004, *J. Atm. and Sol.-Ter. Phys.* **66**, 1295.
- Arge, C. N. and Pizzo, V. J.: 2000, *J. Geophys. Res.* **105**, 10465.
- Bevington, P. R. and Robinson, D. K.: 2003, *Data Reduction and Error Analysis for the Physical Sciences*, 3rd ed., McGraw-Hill, Boston.
- Gosling, J. T.: 1996, *Annu. Rev. Astron. Astrophys.* **34**, 35.
- Harvey, J., Krieger, A. S., Timothy, A. F., and Viana, G. S.: 1975, *Oss. Mem. Oss. Arcetri* **104**, 50.
- Harvey, K. L., and Recely, F.: 2002, *Solar Phys.* **211**, 31.
- Henney, C. J., Harvey, J. W.: 2005, in Large Scale Structures and their Role in Solar Activity ASP Conference Series, K. Sankarasubramanian, M. Penn and A. Pevtsov (eds), **346**, 261.
- Hewish, A., Scott, P. F., and Wills, D.: 1964, *Nature* **203**, 1214.
- Kojima, M., Fujiki, K., Hirano, M., Tokumaru, M., Ohmi, T., and Hakamada, K.: 2004, in The Sun and the heliosphere as an Integrated System, G. Poletto and S. T. Suess (eds), Kluwer Academic Publishers, Chapter 6, 147.
- Kojima, M., Fujiki, K., Ohmi, T., Tokumaru, M., Yokobe, A., and Hakamada, K.: 2001, *J. Geophys. Res.* **106**, A8, 15677.
- Krieger, A. S., Timothy, A. F., and Roelof, E. C.: 1973, *Solar Phys.* **29**, 505.
- Munro, R. H., and Withbroe, G. L.: 1973, *Astrophys. J.* **176**, 511.
- Nolte, J. T., Krieger, A. S., Timothy, A. F., Gold, R. E., Roelof, E. C., Vaiana, G., Lazarus, A. J., Sullivan, J. D., and McIntosh, P. S.: 1976, *Solar Phys.* **46**, 303.
- Sheeley, N. R., Jr. and Harvey, J. W.: 1981, *Solar Phys.* **70**, 237.
- Sheeley, N. R., Jr., Harvey, J. W., and Feldman, W. C.: 1976, *Solar Phys.* **49**, 271.
- Snyder, C. W., Neugebauer, M., and Rao, U. R.: 1963, *J. Geophys. Res.* **68**, 6361.
- Taylor, J. R.: 1997, *An Introduction to Error Analysis; The Study of Uncertainties in Physical Measurements*, 2nd ed., University Science Books, Sausalito, California.
- Wang, Y.-M. and Sheeley, N. R., Jr.: 1990, *Astrophys. J.* **355**, 726.
- Wang, Y.-M. and Sheeley, N. R., Jr.: 1992, *Astrophys. J.* **392**, 310.
- Woch, J., Axford, W. I., Mall, U., Wilken, B., Livi, S., Geiss, J., Gloeckler, G., and Forsyth, R. J.: 1997, *Geophys. Res. Lett.* **24**, 2885.

